Special Section: UZIG USGS
Vadose Zone Journal

Untangling Diffusion from Advection in Unsaturated Porous Media: Experimental Data, Modeling, and Parameter Uncertainty

Philip H. Stauffer,* Jasper A. Vrugt, H. Jake Turin, Carl W. Gable, and Wendy E. Soll

We conducted a series of experimental and modeling tests using data from the Busted Butte Unsaturated Zone Transport Test. First, we conducted a suite of reactive (e.g., Li), nonreactive (Br), and colloidal tracer experiments. These tracers were injected for 190 d from two point sources at rates of 1 and 8 mL/h, respectively. We then used a numerical simulator (FEHM), populated with laboratory-measured hydrologic properties, to verify that our conceptual model of the tracer test yielded a good fit to the tracer breakthrough data. Additionally, we used the AMALGAM-SO and SCEM-UA search algorithms to find optimal parameter estimates in our conceptual model and estimate their (nonlinear) uncertainty. To this end, the FEHM model was executed more than 50,000 times using parallel computing on a distributed computer cluster. The experimental and modeling results show that (i) no breakthrough of colloids was observed, low breakthroughs of Li were found, and significant and rapid breakthrough of Br was measured, (ii) measured hydraulic parameters from rock core samples provide a relatively accurate description of flow and transport at the scale and flow rates of the Busted Butte test, and (iii) the Millington–Quirk model of diffusion as a function of volumetric water content can fit the experimental breakthrough data well; however, (iv) a constant diffusion model with a much lower effective diffusion coefficient also fits the data well, and (v) numerous different optimized parameter combinations exist that fit the observed Br data acceptably well. This implies that one should be particularly careful in assigning values of the unsaturated subsurface flow and transport parameters without recourse to examining both parameter and model formulation uncertainty.

Abbreviations: FEHM, finite element heat and mass transfer porous flow simulator; LANL. Los Alamos National Laboratory; SCEM-UA, Shuffled Complex Evolution Metropolis algorithm.

Yucca Mountain is being studied extensively to determine whether it is a suitable site for a high-level nuclear waste repository. In particular, much research has been conducted on the hydrologic and geochemical properties of the vadose and saturated zones surrounding Yucca Mountain (Robinson and Bussod, 2000). Experiments have been performed at the proposed waste storage horizon in the Exploratory Science Facility; however, rocks below this level are difficult to access within Yucca Mountain (Bechtel SAIC Company, 2004a,b).

The Busted Butte Unsaturated Zone Transport Test (UZTT) was designed to access exposures of the Topopah Spring Tuff and the Calico Hills Tuff, units stratigraphically correlative and mineralogically similar to the unsaturated rocks underlying the proposed repository (Robinson and Bussod, 2000; Turin et al., 2002). Busted Butte is located at the Nevada Test Site, approximately 160 km northwest of Las Vegas, NV, and 8 km southeast of Yucca Mountain. The UZTT was initiated to explore the in situ behavior of solute and colloid movement through the tuff horizons that underlie the proposed repository. Specific issues of concern include the interaction of solute and colloid transport with heterogeneity and fractures, applicability of measured laboratory parameters to the field scale and site scale, and evaluation of numerical models for unsaturated transport in fractured tuff.

The Busted Butte UZTT consisted of three phases of in situ tracer injection and breakthrough analysis. Phases 1A and 1B were designed as multicomponent scoping studies to aid in the design and analysis of the later Phase 2 experiment. Phase 1 tests consisted of parallel pairs of injection and collection boreholes that essentially captured three-dimensional flow on the scale of a meter or less. Phase 1A, described in Robinson and Bussod (2000), was designed to capture the qualitative aspects of unsaturated zone transport at this site. The objective of Phase 1B was to identify the dominant physical processes controlling solute transport through unsaturated tuff at low flow rates across submeter distances and to determine whether the hydrogeologic properties of rocks measured in the laboratory are useful in describing the behavior of rocks in the field. Additionally, Phase 1B was located to include a naturally occurring fracture within the test block, providing insight into our understanding of the role of fractures on transport in the Topopah Springs Tuff at low flow rates. Phase 2 was run to explore transport in a larger three-dimensional block using an array of perpendicular injection and collection boreholes as well as a larger range in injection rates. A primary conclusion from numerical modeling of both Phase 1A and Phase 2 is that capillary forces are sufficient to explain much of the flow and

P.H. Stauffer, J.A. Vrugt, H.J. Turin, C.W. Gable, and W.E. Soll (deceased), Los Alamos National Lab., P.O. Box 1663, Los Alamos, NM 87545. Received 5 Mar. 2008. *Corresponding author (stauffer@lanl.gov).

Vadose Zone J. 8:510–522
doi:10.2136/vzj2008.0055

transport in the test block (Robinson and Bussod, 2000; Tseng et al., 2003).

We investigated tracer breakthrough data from Phase 1B of the Busted Butte UZTT with observations of probable influences from experimental design and sampling techniques. The finite element heat and mass transfer porous flow simulator (FEHM; Zyvoloski et al., 1997; Zyvoloski, 2007), populated with laboratory-measured hydrologic properties, was then used to verify that our conceptual model of transport through unsaturated tuff can reproduce the Phase 1B tracer data. The finite element heat and mass transfer porous flow simulator solves multiphase fluid flow and tracer transport on a numerical grid representing the domain of the tracer test at the Busted Butte field site.

We conducted a number of different optimization runs to fully explore the parameter space and better understand the optimized values of the parameters. To this end, we conducted a parallel implementation of AMALGAM-SO (Vrugt et al., 2008) to find the best attainable values by sampling a broad range of porosity, saturation, van Genuchten's n and α, the horizontal and vertical permeability, and the effective porous medium diffusion coefficient of the rock. Unfortunately, this optimization finds a single best parameter combination without recourse to examining the uncertainty associated with this solution. Thus, in a second step, we use the Shuffled Complex Evolution Metropolis (SCEM-UA) global optimization algorithm developed by Vrugt et al. (2003a,b) to densely sample the parameter space in the vicinity of the global optimum. This exhaustive evaluation of the solution space was used to estimate parameter uncertainty and correlation and therefore provides important insights into which processes in FEHM are very well understood and which processes are not very well understood at the Busted Butte field site.

Hydrogeologic Setting

Busted Butte lies in the north-central part of the Basin and Range physiographic province, which is characterized by extensional tectonism and magmatism active during the Middle and Late Cenozoic eras (Stuckless and Dudley, 2002). Busted Butte is a small (2.5 by 1 km) mountain block composed of the Miocene Paintbrush Group (Scott and Bonk, 1984). The Busted Butte Test Site is located within a horst bound by the Paintbrush Canyon Fault on the west and the Busted Butte Fault on the east (Bussod et al., 1998). The Busted Butte test block lies in the unsaturated zone within the Topopah Spring Tuff unit of the Paintbrush group, a moderately to densely welded, rhyolitic ash-flow tuff dated at 12.8 million yr. It is divided into two units, a lower crystal-poor unit (Tptpv1) and an upper crystal-rich unit (Tptpv2). The tuff is compositionally zoned, with high-silica rhyolite in Tptpv1 and quartz latite in Tptpv2 (Stuckless and Dudley, 2002). The Tptpv2 unit consists of a tan, partly welded ignimbrite with columnar jointing. Pumice clasts are typically 1 to 6 cm in their long dimension and exhibit flattening ratios from 6:1 to 8:1. The matrix consists of black glass shards in a tan ashy matrix. Welding increases upsection (Bechtel SAIC Company, 2004b). The Phase 1B tracer test block is located in the lower part of Tptpv2 just above the contact between the two units.

Tracer Test Design

The underground test facility constructed at Busted Butte consists of a 75-m main adit and a 19-m test alcove perpendicular to the adit. The excavated adit provided access to exposed surfaces of the Topopah Springs and Calico Hills tuffs. Construction was coordinated to ensure minimal disturbance of the in situ test block. To limit evaporation from the test region, shotcrete and sodium silicate glass were applied to the tunnel walls and an airlock was constructed at the entryway.

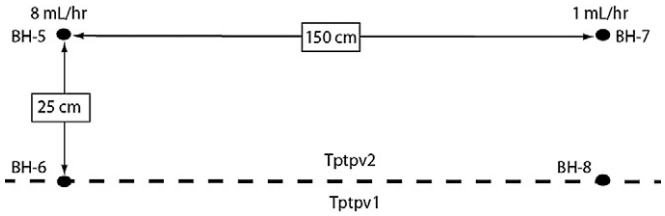

FIG. 1. Phase 1B geometry on the vertical drilling face of the alcove, showing the relative locations of the injection boreholes (BH-5 and BH-7), collection boreholes (BH-6 and BH-8) and the tuff units Tptpv2–Tptpv1 contact.

Before testing, numerous rock and pore water samples were collected from nearby outcrops and from the tunnel. Pore water and rock samples were analyzed at the Los Alamos National Laboratory (LANL) for their chemical composition and lithologic and mineralogic properties (Turin et al., 2002). These samples were used to characterize the lithology and to create synthetic pore water for use in the tracer test.

Phase 1B made use of four horizontal, 2-m-long, 0.1-m-diameter boreholes. Figure 1 shows a vertical cross-section of the drilling face with stratigraphy and the relative locations of the different boreholes within the Phase 1B test. Tracer injection began with an average injection rate of 8 mL/h in Borehole 5 and 1 mL/h in Borehole 7. Injection in Borehole 7 was terminated after 181 d, while injection in Borehole 5 was terminated after 190 d.

A variety of nonreactive, reactive, and colloidal tracers (Table 1) were injected simultaneously to provide a range of breakthrough data to help validate our conceptual models for the different styles of transport at this site. Additionally, the simultaneous use of multiple tracers with different transport properties is likely to increase information retrieval from the subsurface and should better constrain the various parameters that are necessary for accurate prediction of flow and transport. Turin et al. (2002) provided a detailed discussion of the criteria used to select each tracer. Bromide is a nonreactive tracer and should move with the injected water. A nonreactive tracer in the context of this study means that no significant quantity of the tracer interacts with the rock during the time of the experiment, while a reactive tracer showed measurable retardation in controlled laboratory tracer studies (Anghel et al., 2002; Turin et al., 2002). Sodium fluorescein and pyridone are also nonreactive

TABLE 1. Composition of the Phase 1B tracer solution.

Tracer	Concentration
LiBr	500 ± <5 mg/L
Sodium fluorescein (uranine, acid yellow 73)	500 ± <5 mg/L
Pentafluorobenzoic acid in Borehole 7	100 ± <1 mg/L
2,6-difluorobenzoic acid in Borehole 5	100 ± <1 mg/L
Carbomoyl-2(1*H*)-pyridone	100 ± <1 mg/L
Fluorescent polystyrene microspheres	1 ± <0.01 mL/L

and were used as markers that could be detected in the field using ultraviolet illumination at concentration levels of approximately 10 mg/kg. Pentafluorobenzoic acid and 2,6-difluorobenzoic acid (2,6-diFBA) are nonreactive tracers and were used to tag the two injection boreholes according to injection rates (i.e., 8 and 1 mL/h rates, respectively) in the event that injection from one test reached the receptor pads for the other test. Lithium was chosen as a weakly sorbing tracer. Fluorescent polystyrene latex microspheres of two sizes (0.3- and 1-μm diameter) were used as colloid tracers. To minimize the reactivity of the tracer solution with country rock, synthetic pore water based on the measured in situ composition was used (Turin et al., 2002).

Injection and sampling of tracers was accomplished using two pneumatically inflated borehole sealing and measurement systems (Tseng and Bussod, 2001; Turin et al., 2004). Tracer solution was pumped from a tank into the injection boreholes and delivered to a fabric pad, held in place by the packer, which helped to confine the flow to a well-defined injection point at 130 cm into each borehole. Moisture sensors were mounted on the outside of the packers at each injection port to monitor both ambient and injection moisture levels. Sensors consisted of two wires separated a fixed distance apart and embedded in the pad assembly, and the resistance between these two wires was measured using a datalogger (Bechtel SAIC Company, 2004b). The packers were made of transparent material to allow visual inspection of the injection points and borehole geology with both standard and ultraviolet illumination.

Pore-water samples were collected from Boreholes 6 and 8 (Fig. 1) using absorptive filter paper pads and an inverting membrane. The inverting membranes consisted of welded tubes of double-coated polyester fabric 0.1 m in diameter. A mesh pocket ran the length of each membrane to hold the sampling pads in place. Each pad consisted of a bundle of 10 disks of Whatman no. 42 filter paper approximately 0.047 m in diameter, and pads were located along the borehole at approximately 10-cm intervals. The membranes were removed and replaced every 1 to 2 wk. After removal, the pads were packaged individually in 60-mL amber Nalgene bottles and shipped to LANL for analysis. Bromide and the fluorobenzoic acids were extracted from the pads using a bicarbonate–carbonate buffer solution, and Li was extracted using 2% HNO_3. A total of 176 pads were extracted for tracers, and the extracts were analyzed by ion chromatography, inductively coupled plasma–mass spectrometry, high performance liquid chromatography, spectrofluorimetry, and epifluorescent microscopy. The total moisture content of the pads was determined by oven drying. Tracer concentrations were determined by dividing the mass of a given tracer from the extraction by the total moisture content of that sample. Turin et al. (2004) described the extraction technique in more detail.

Tracer Breakthrough Measurements

Breakthrough of all five solute tracers was detected in Borehole 6, directly beneath the 8 mL/h injection site in Borehole 5. No breakthrough was detected in Borehole 8, which is situated below the 1 mL/h injection site in Borehole 7. No clear evidence of microsphere breakthrough was detected in either borehole.

All five tracers observed in Borehole 6 showed peak concentrations at a horizontal distance of approximately 130 cm from the end of the borehole, directly below the injection port

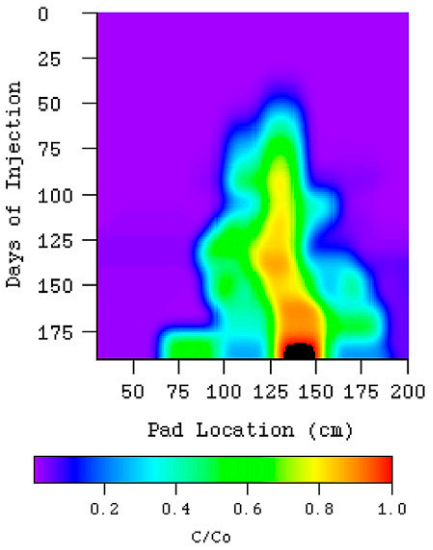

FIG. 2. Concentration contour plot for Br breakthrough in Borehole 6; C_o is the concentration of Br in the injection solution (460 mg/kg).

in Borehole 5; however, the maximum recovery of a given tracer at a given collection point varied greatly in Borehole 6. Bromide and 2,6-diFBA, both anionic nonreactive tracers, showed similar and reasonable breakthrough patterns, with initial breakthrough detected after approximately 1 mo of injection. Both Br and 2,6-diFBA reached 50% injection concentrations after 2 mo of injection. Bromide breakthrough results are shown in Fig. 2.

In contrast to Br, the fluorescein breakthrough pattern was more erratic. In particular, the peak concentration measured was more than twice the injection concentration. This anomalous behavior may reflect analytical difficulties associated with the extremely high concentration of fluorescein injected, combined with matrix effects on sample fluorescence; however, the high concentrations of fluorescein succeeded in improving field visualization of the injected tracer. Pyridone showed later breakthrough than the other conservative tracers (>100 d); however, Turin et al. (2002) showed that pyridone is nonreactive at Busted Butte, so these results are thought to reflect analytical difficulties.

Lithium results are shown in Fig. 3. Low (normalized concentration $C/C_o = 0.04$) and late (190 d) breakthrough is interpreted as Li sorbing and thus being significantly retarded with respect to Br. Although the measured Li concentrations were quite low,

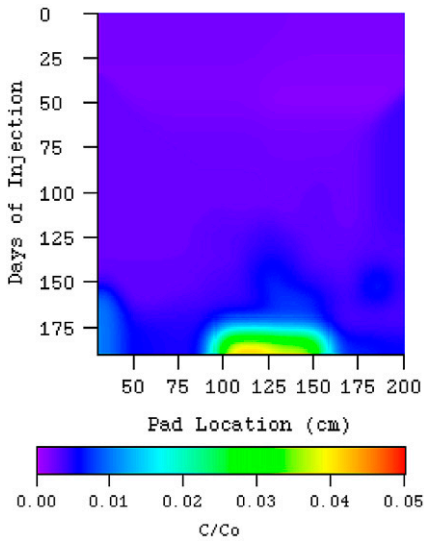

FIG. 3. Concentration contour plot for Li breakthrough in Borehole 6; C_o is the concentration of Li in the injection solution (40 mg/kg).

their contrast with background levels and their consistent location both in time and space indicate that Li breakthrough was indeed observed in the field.

A qualitative discussion of the Phase 1B tracer results can be found in Robinson and Bussod (2000). They asserted that, although the earliest breakthrough occurred at the location of the fracture that connects Borehole 5 to Borehole 6 (at 130 cm in from the drilling face, Fig. 2), the first arrival of Br at the collector in Borehole 6 was between 28 and 35 d, far longer than would be expected if flow had been channeled preferentially through the fracture based on a reasonable increase in fracture permeability. Additionally, Br was detected in <100 d in lateral collector pads located up to 30 cm away from the fracture plane (Fig. 2). The conclusion that the fracture at this site is not contributing significantly to flow and transport is also supported by Bechtel SAIC Company (2004a). Because the previous work concluded that the fracture located within the test block played little to no role in flow or transport, we do not further discuss fracture flow with respect to Phase 1B.

We used the tracer data to constrain numerical models that were designed to provide insight into hydrologic parameterization at the scale of the Busted Butte test bed.

Tracer Test Conceptual Model

Model Domain

To simplify the numerical analysis, the test block was conceptualized as a vertical cylinder with a radius of 0.5 m and a height of 1.5 m. Assuming radial symmetry, the test block was simplified as a radial plane that was projected around the vertical axis to solve the equations of flow and tracer transport in a three-dimensional volume (Fig. 4). The test cylinder was divided into two lithologic units along the assumed horizontal contact between Unit 2 and Unit 1 of the Topopah Springs Tuff. Each lithologic unit was assumed to be homogeneous. As a result of the simplified radial geometry, the injection and collection boreholes were modeled as spheres along the central axis of the cylinder. The injection pad was explicitly included in the bottom of Borehole 5. The collection pad located directly beneath the injector was explicitly included at the top of Borehole 6. These modifications are relatively minor and the numerical grid captures the volume and radial nature of the experimental flow much more closely than a two-dimensional Cartesian representation. The approximation of radial symmetry introduces more spherical flow than would be simulated in a true three-dimensional representation of the domain; however, the effect is fairly small and quantifiable. We calculated that the radial symmetry assumption provided 3.5% more volume for the injected water to move into; however, this slight change in volume does not significantly change any of our conclusions.

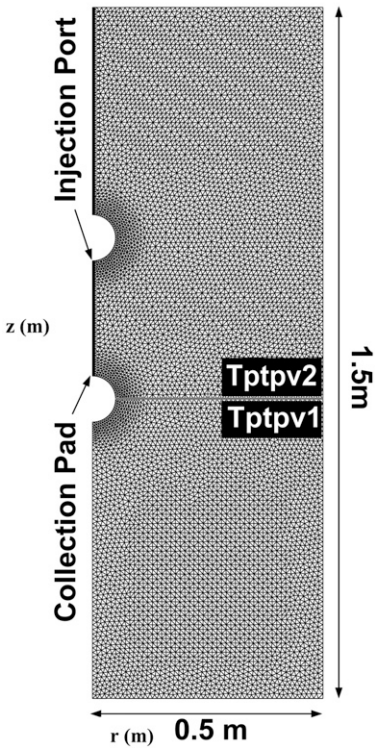

FIG. 4. Model domain with the numerical grid shown and the tuff units Tptpv2–Tptpv1 contact. Injection occurred at radius r = 0.0 and elevation z = 0.95 m and the axial collector is located at r = 0, z = 0.7 m.

Flow and Transport Models

Unsaturated water flow was modeled using the water retention relationships of van Genuchten (1980), and the following two equations describe the relative permeability and capillary pressure functions that were used in this study:

$$R_l = \sqrt{S}\left[1.0 - \left(1.0 - S^{1/m}\right)^m\right]^2 \quad [1]$$

$$P_{cap} = \frac{1}{\alpha}\rho_l g\left(S^{-1/m} - 1.0\right)^{1.0-m} \quad [2]$$

where m (dimensionless) = (1 – 1/n), R_l (dimensionless) is the relative permeability multiplier for the liquid water saturated permeability, S (dimensionless) is the saturation, P_{cap} (Pa) is the capillary pressure, ρ_l (kg/m^3) is the liquid water density, g (m/s^2) is the magnitude of the gravitational force vector, and α (m^{-1}) and n (dimensionless) are experimentally determined fitting parameters.

We assumed that advective fluid flow is driven by the sum of the matric and gravitational potentials and can be represented using a two-phase formulation of Darcy's law for the movement of both water and air (Stauffer and Rosenberg, 2000; Zyvoloski et al., 1997). Characteristic curves were generated by optimizing laboratory data to the van Genuchten–Mualem model, described in more detail by Tseng et al. (2003). Solute transport was described by the advection–dispersion equation, with modifications to include sorption (Fetter, 1999). In this theory, tracer migration is controlled by bulk water flow, mechanical mixing (dispersion), chemical reactions, and molecular diffusion. In unsaturated porous media, the molecular diffusion coefficient can be expressed as a function of volumetric water content because the random motions that cause diffusion are restricted to ever more tortuous pathways as water content decreases (Millington and Quirk, 1961).

Tracer Chosen for Simulation

Bromide was chosen for the solute transport modeling study because it was the most robust of the nonreactive tracers and showed the most stable breakthrough from the experimental data. Lithium was evaluated for use in this study as the reactive tracer; however, breakthrough levels were considered too low to be useful

in modeling. The free water diffusion coefficient for Br is 2.09 × 10^{-9} m^2/s at 20°C (Fetter, 1999).

Models for Diffusion as a Function of Water Content

A porous medium diffusion coefficient, D^* (m^2/s), was used in the model to account for the tortuosity of the porous medium, which reduces the ability of a chemical to diffuse through the water in the pore spaces (Clennell, 1997). This parameter should not be confused with the matrix diffusion parameter used in large-scale simulations to account for interaction between fractures and the surrounding porous medium (Liu et al., 2005). We investigated two alternate functions from the literature that are commonly used to calculate diffusion as a function of volumetric water content and converted them into formulations that could be used in the simulations.

The first function is based on a modified version of the Millington–Quirk (MQ) tortuosity relationship (Jury and Gardner, 1991) and calculates an effective diffusion coefficient, D_{eff} (m^2/s), as

$$D_{eff} = \frac{D_{free}\theta_w^{10/3}}{\phi^2} \quad [3]$$

where D_{free} is the free-water diffusion coefficient, θ_w (m^3/m^3) is the volumetric water content, defined as the volume of water divided by the total volume of rock, and ϕ (dimensionless) denotes the porosity.

The second function that we explored was adapted from Conca and Wright (2000), here referred to as the CW model. Their formulation is based on measurements using the Unsaturated Flow Apparatus (UFA) and covers a range of soil and rock types for solutions of NaCl and KCl. The UFA does not directly measure diffusion; however, it measures electrical current in an essentially uniform water content so that the Nernst–Einstein equation can be used to estimate D_{eff}. A good fit to the UFA data is expressed (in m^2/s) as (adapted from Conca and Wright, 2000)

$$D_{eff} = 10^{-8.1+2.7(\log\theta_w)+0.32(\log\theta_w)^2} \quad [4]$$

Figure 5A shows values of D_{eff} calculated using these two models. At high volumetric water contents, the models break down, giving values that are close to the free-water diffusion coefficient. Both Eq. [3] and [4] are based on solution of the steady-state equation for contaminant flux (Fick's first law):

$$J = D_{eff}\nabla C \quad [5]$$

where C is the concentration (mol/L) and J is the solute flux [mol/(m^2 s)] (Stauffer, 2006). The finite element heat and mass transfer porous flow simulator and other porous flow simulators generally use the following equation for solute flux that explicitly removes volumetric water content, isolating the diffusion coefficient that is seen by chemicals within the liquid-filled pores (Ho and Webb, 1998):

$$J = \theta_w D^* \nabla C \quad [6]$$

leading to a relationship between the porous medium diffusion coefficient, D^*, and reported values of D_{eff} as

$$D^* = \frac{D_{eff}}{\theta_w} \quad [7]$$

Figure 5B shows values of D^* calculated from both the MQ and CW models. The values at any volumetric water content are higher than the values calculated using Eq. [3] and [4]. Because Eq. [5] does not separate the water content from the actual porous medium diffusion coefficient, one cannot simply substitute D_{eff} into Fick's second law. The correct form of Fick's second law for partially saturated porous media is expressed as (Bear and Verruijt, 1989, Eq. 6.3.2; Fetter, 1999, Eq. 4.33)

$$\frac{d\theta_w C}{dt} = \nabla\cdot J = \nabla\cdot\theta_w D^*\nabla C \quad [8]$$

Substituting J from Eq. [5], we arrive at

$$\frac{d\theta_w C}{dt} = \nabla\cdot D_{eff}\nabla C \quad [9]$$

This can be rewritten, assuming that volumetric water content is not changing locally, in the more traditional form as

$$\frac{dC}{dt} = \nabla\cdot\frac{D_{eff}}{\theta_w}\nabla C = \nabla\cdot D^*\nabla C \quad [10]$$

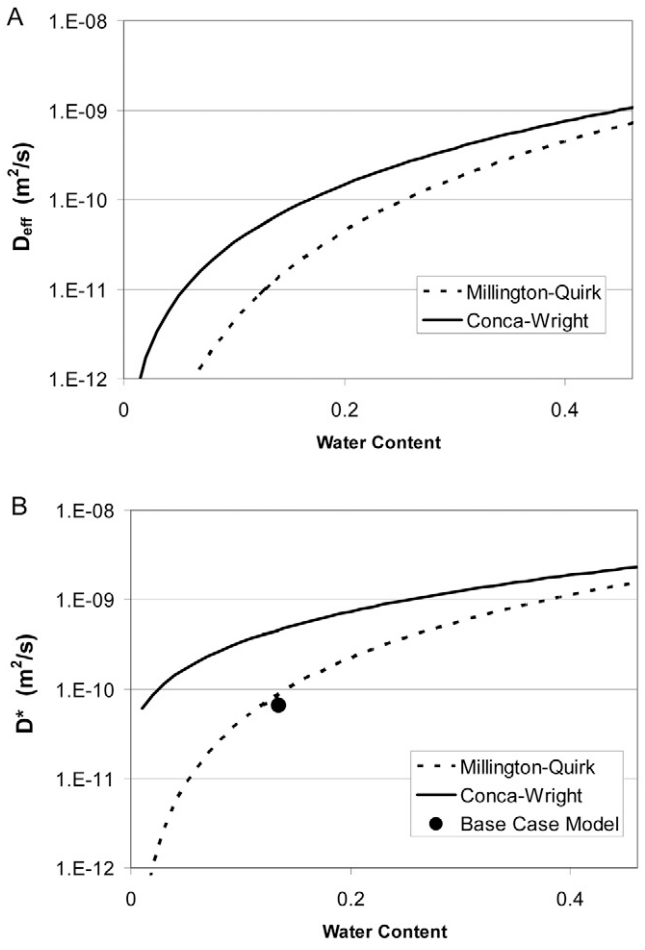

FIG. 5. Comparison of the Millington–Quirk and Conca–Wright formulations for (A) the effective diffusion coefficient, D_{eff}, from Eq. [5], and (B) the porous medium diffusion coefficient, D^* from Eq. [6]. The porosity used in the calculation of the Millington–Quirk curve (ϕ = 0.463) is from the base case model (Table 2).

Equation [10] shows that the time rate of change of concentration in the saturated pores is actually a function of D^* and is not represented by D_{eff} alone. This subtle point is often missed in modeling exercises and has led to confusion in the literature (Fetter, 1999, compare Eq. 4.28 and 4.29). For example, Karimi et al. (1987) showed very good matches to Millington–Quirk for a steady-state experiment that measured D_{eff}; however, time-dependent estimates of an effective diffusion coefficient will yield measurements of D^* that are greater than steady-state D_{eff} values (Schaefer et al., 1995). The discrepancy between D^* and D_{eff} is also found in estimates of the gaseous diffusion coefficient derived using similar methods, and care must be taken when converting steady-state measured values in the literature for use in time-dependent numerical simulators (Schaefer et al., 1997; Stauffer et al., 2005).

Hydrologic Data Incorporated in the Simulations

Core samples collected from Busted Butte were used to make laboratory-scale measurements of the hydraulic and physical properties of the rock units found at Busted Butte (e.g., Flint, 1999). The measured retention and hydraulic conductivity values were then optimized and used to simulate the Busted Butte Phase 2 tracer transport test (Tseng et al., 2003). In this study, we used the geometric mean of the Tptpv1 and Tptpv2 measured hydraulic conductivity data (Flint, 1999) combined with the optimized values of residual water content, and van Genuchten α and n values for Tptpv1 and Tptpv2 from Tseng et al. (2003). These optimized values are from a joint calibration to both retention data (51 core samples) and hydraulic conductivity data (28 core samples). We also used the calibrated porosity values from Tseng et al. (2003) based on the hydraulic conductivity optimization (see also Bechtel SAIC Company, 2004a). Because Phase 2 was conducted at the same location, we assumed that the calibrated values for the hydrologic properties are applicable to the Phase 1B test.

Target saturation values for Tptpv1 and Tptpv2 were based on neutron probe measurements collected in the Phase 1A and 1B boreholes before injection. The physical and hydraulic properties of the injection and collection pads are from laboratory studies on the pad material (Science and Engineering Associates, 1992). Table 2 summarizes these data.

Simulations of Flow and Transport

Finite-Volume Porous Flow and Transport Code

We used the Los Alamos porous flow simulator, FEHM, for all calculations in this study (Zyvoloski et al., 1997; Zyvoloski 2007). It is a finite-volume heat and mass transfer code that has been used extensively for simulation of multiphase flow and transport in the unsaturated zone (Tseng et al., 2003; Neeper and Stauffer, 2005a; Stauffer and Stone, 2005). The governing equations in FEHM were derived from the principles of conservation of mass and energy (Zyvoloski et al., 1997; Stauffer and Rosenberg, 2000). Darcy's law is assumed to be valid for the flow of the air and water phases. Solute transport in FEHM is governed by the advection–dispersion equation. For a discussion of the assumptions regarding solute transport incorporated into the numerical model, see Viswanathan et al. (1998). The code has been modified to include constant porous medium diffusion (CD) and both the MQ and CW formulations for water and vapor tracer diffusion as functions of water content (Kwicklis et al., 2006).

Computational Grid

The model domain was a radial cross-section of the test cylinder, 0.5 m in radius and 1.5 m in height. The grid was generated using the LaGrit software (Trease et al., 1996) and consisted of 9584 nodes and 18,602 triangular elements. Grid spacing was more refined near the injection and collection pads as well as around the boreholes (Fig. 4). As stated above, the grid was meant to represent a reasonably close approximation of the field experiment. Furthermore, to differentiate between the effects of diffusion and advection, we required a high grid resolution that minimized numerical dispersion in the advection–dispersion equation. The grid we used was designed to yield numerical dispersion on the order of 0.01 m, approximately what one would estimate from relations between dispersivity and path length (Fetter, 1999).

Boundary and Initial Conditions

The top and bottom of the domain were simulated as constant saturation boundaries. The bottom boundary was far enough below the injector pad to prevent pooling of water at the bottom of the domain. The radial boundary was modeled as having no flow and was assumed to be far enough away from the injection plume to have a minimal effect on flow and transport processes. Average background infiltration fluxes for the deep unsaturated zone in the vicinity of Busted Butte are estimated to be on the order of 1×10^{-3} to 1×10^{-1} cm/yr (Bechtel SAIC Company, 2004a). The coupled numerical model would be overconstrained if one were to fix both the initial saturation (S_{ini}) and the infiltration flux, so we chose to fix saturation at the top of the model to generate steady-state background conditions for the tracer simulations. The FEHM model was initially run for 1 million d to equilibrate the flow field to the boundary saturations at the Busted Butte field site. Thus, a steady-state initial condition was generated for each transport simulation presented below. For all simulations, we used a steady injection rate of 8 mL/h to simulate the average injection rate for Borehole 5 during the experiment. The steady-state background infiltration flux was very low compared with the flux of water created by the 8 mL/h injector. Because of inconsistencies in the late-time experimental data for all species (Bechtel SAIC Company, 2004a), we used the observed data for only the first 100 d.

Table 2. Hydraulic and physical properties used in the base simulation.

Material	$k_h = k_z$	ϕ	S_{ini}	θ_r	α	n	D†
	m^2				1/m		m^2/s
Tptpv2 tuff unit‡	3.53×10^{-13}	0.461	0.29	0.023	1.595	1.300	6.5×10^{-11}
Tptpv1 tuff unit‡	2.73×10^{-13}	0.463	0.22	0.068	0.479	1.541	6.5×10^{-11}
Injection and collection pad§	2.19×10^{-11}	0.85	0.80	0.050	17.0	1.12	6.5×10^{-11}

† Porous medium diffusion coefficient (Eq. [6]). This value is fixed only for the manually calibrated base simulation.

‡ Values of saturated permeability (k_h,k_z) were taken as the geometric mean of 25 and 19 measurements respectively for Tptpv1 and Tptpv2 (from Flint, 1999); initial saturation values (S_{ini}) were taken from moisture sensor data taken before injection; porosity (ϕ) and the van Genuchten model parameters (fitting parameters α and n and residual volumetric water content θ_r) were taken from Tseng et al. (2003).

§ Values are taken from Science and Engineering Associates (1992).

Base Simulation

Table 2 presents our best estimates of the hydrogeologic parameters derived from previous studies using experiments on rock core samples at the experimental field site. These values were used to create a base simulation with FEHM. This first simulation demonstrated whether the previously determined values of the hydrologic parameters for Tptpv2 provided an accurate prediction of the Phase 1B tracer test. First, the base simulation resulted in a background volumetric water content in the Tptpv2 of about 0.13, which is within measured neutron probe values for this site and in agreement with observations of water content presented in Tseng et al. (2003). Second, steady-state infiltration flux in the domain before injection was approximately 0.04 cm/yr, which is well within the range of previously estimated values of background infiltration.

Two variations of the base simulation were considered, one using the MQ model and one using the CW approach for porous medium diffusion as a function of water content. Results from these simulations are shown in Fig. 6, which compares the measured and simulated breakthrough of Br at the collector pad directly beneath the injection port (axial collector). This location corresponds to the collection pad 1.30 m into the borehole. Note that the base simulation using MQ had an initial breakthrough that was very close to the measured concentration data; however, the simulated concentrations consistently overpredicted the measured data, resulting in an RMSE value of about 0.09. The base simulation derived with CW did not fit the observed concentration data very well and greatly overpredicted concentrations in the first 60 d, while underpredicting the data at later times. The ratio of the porous medium diffusion coefficient at the in situ water content for the CW and MQ models is about 5.3, which explains why the CW model is more diffusive than the MQ model. This is quantitatively in good agreement with the results presented in Fig. 5.

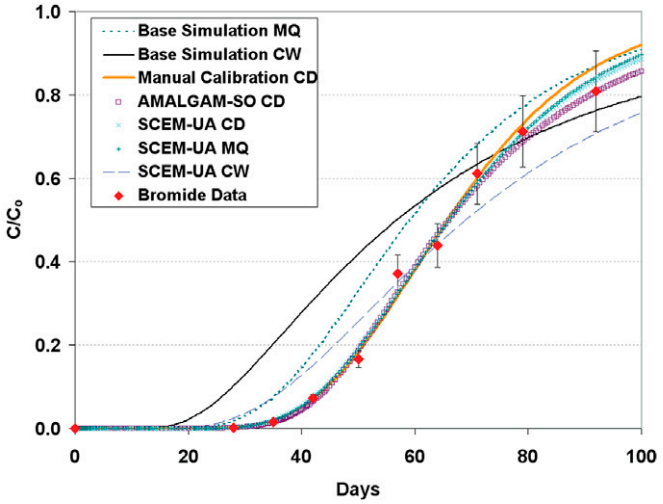

FIG. 6. Data compared with results of the base simulation using both the Millington–Quirk (MQ) and Conca–Wright (CW) diffusion models, the manual calibration with a constant diffusion (CD) coefficient (D^* = 6.5 × 10^{-11} m^2/s), optimization using AMALGAM-SO with a CD coefficient, and Shuffled Complex Evolution Metropolis (SCEM-UA) optimizations for CD and the MQ and CW diffusion models. Error bars on the data represent overall reproducibility of approximately 12% for individual measurements.

We next performed a manual calibration by tuning the Br porous medium diffusion coefficient (D^*) to find the best fit to the measured Br breakthrough data using the base values of the other parameters as presented in Table 2. To simplify our analysis, the diffusion coefficient was modeled as a constant value (CD) and not as a function of the volumetric water content. This manual calibration resulted in an optimized diffusion coefficient of D^* = 6.5 × 10^{-11} m^2/s or D_{eff} = 7.68 × 10^{-12} m^2/s, and yielded a much improved fit to the experimental breakthrough data with an RMSE of about 0.026 (Fig. 6). Note, however, that the diffusion coefficient that was derived with this approach is approximately 1.3 times lower than that calculated using the MQ model and seven times lower than the CW model.

Contributions of Advection and Diffusion to Total Transport

It was vital to simulate both advective and diffusive transport to capture the observed breakthrough in this experiment. The solute flux of a nonreactive tracer through a porous medium consists of two terms—the advective term and the dispersive term:

$$J = qC + D'\nabla C \quad [11]$$

where q is the volumetric flux [m^3 water/(m^2 s)] and D' (m^2/s) is the dispersivity tensor. Hydrodynamic dispersion is further decomposed into two terms: the product of the dispersivity [α_{disp} (m)] and the true fluid velocity [ν (m/s)], plus porous medium diffusion as

$$D' = \alpha_{disp}\nu + \theta_w D^* \quad [12]$$

During initial breakthrough, advection was limited to a region near the injector (Fig. 7). Figure 8 shows the corresponding

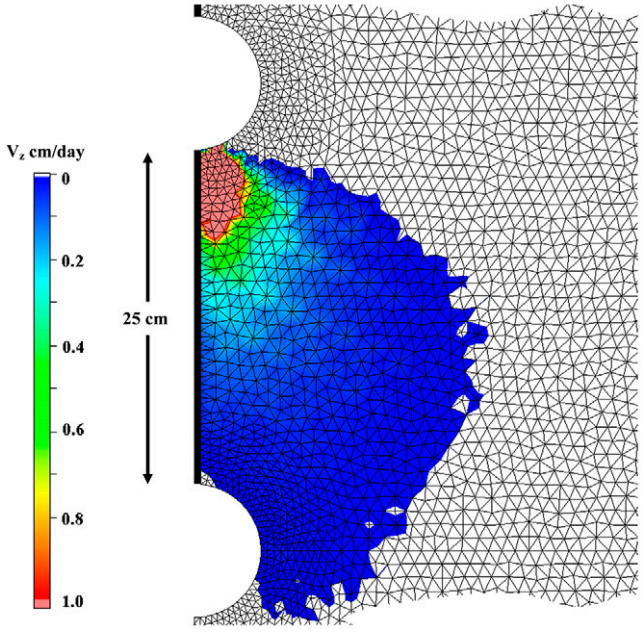

FIG. 7. Magnitude of the vertical liquid volume flux vector (V_z) for the manual calibration simulation after 27.8 d of injection. The view is zoomed in on the region between the simulated injection point and the simulated collection pads and the grid has been truncated.

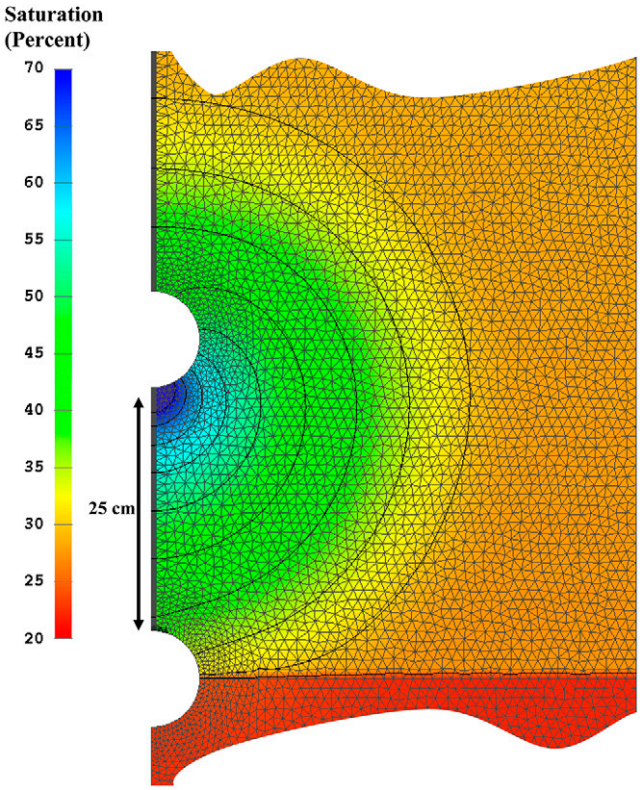

FIG. 8. Saturation profile for the manual calibration after 27.8 d of injection. The view is zoomed in on the region of interest and the grid has been truncated.

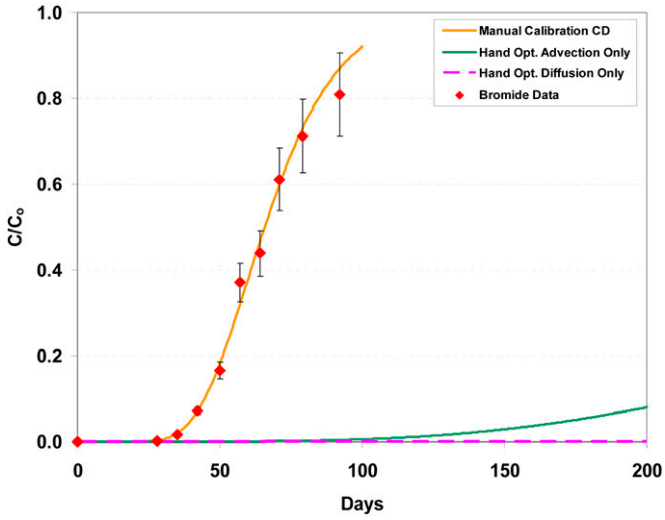

FIG. 9. Comparison of molecular diffusion and advection. With no injection and only diffusion, the tracer does not break through. With no diffusion and only advective transport, the tracer breaks through only at a later time and at very low concentrations. Error bars on the data represent an overall reproducibility of approximately 12% for individual measurements. The base case with constant diffusion (CD) and the data are shown for reference.

saturation profile in the domain at initial breakthrough. Below the region of advective flux, D' was dominated by molecular diffusion. To highlight the need to include both diffusive and advective transport in the simulated experiment, we ran two simulations that changed only a single part of the manual calibration. The first simulation fixed the solute concentration at the injection borehole with no fluid injected, such that diffusion became the only transport mechanism. The second simulation reduced D^* to zero, so that advection was the only mechanism contributing to transport. Figure 9 shows that as D_{eff} was reduced to zero, the amount of mass transported to the collection pad decreased to near zero. For the diffusion-only case, tracer did not reach the receptor pad in 200 d. For the advection-only case, breakthrough occurred after approximately 100 d; however, C/C_o at the collection pad remained below 10% throughout the 200 d of the simulated tracer test. Thus, the total transport seen in the data requires both an advective component, which moves a region of higher saturation and concentration toward the receptor pad, and a diffusive component, which brings mass from the advectively dominated region to the receptor.

Optimization Using AMALGAM-SO

Although our model simulations closely matched the observed Br concentration data, the parameters we used differ substantially from values found in a previous optimization of the Phase 1B Br breakthrough data (Table 3). Bechtel SAIC Company (2004a) admitted that their optimized permeability values of the Tstpv2 unit make little physical sense when compared with their independently measured values. In fact, they differ by orders of magnitude. To better understand why such widely varying values in the optimized parameters have been obtained in different studies using the same data set, we used a robust new multimethod evolutionary search methodology, entitled AMALGAM-SO, which was recently developed at LANL (Vrugt and Robinson, 2007a; Vrugt et al., 2008, 2009). This method facilitates finding the global minimum in the search space, and thus will reduce ambiguity about the values of the optimized parameters.

Using a parallel version of AMALGAM-SO (Vrugt et al., 2008, 2009), we performed >12,000 FEHM model simulations, allowing parameters to vary between the bounds listed in Table 4. The ranges for saturation and porosity were taken from data reported in Tseng et al. (2003). We chose the bounds for the initial AMALGAM-SO optimization runs to be very broad to allow finding solutions in the parameter space set forth in work by Bechtel SAIC Company (2004a) and Tseng et al. (2003). The objective function that we minimized is the residual between the model and measured data at each of the data points shown in Fig. 6.

TABLE 3. Optimized parameter combinations† found for the Tptpv2 tuff unit for Bechtel SAIC Company (2004a,b) (BSC) and AMALGAM-SO. In the BSC study, k_x and k_y are independent horizontal permeability components and x and y directions, respectively, while in this study the radial symmetry of the simulations results in $k_x = k_y = k_h$.

Study	k_x	k_y	k_z	ϕ	S_{ini}	α	n	D^*
	m^2					1/m		m^2/s
BSC	3.1×10^{-17}	4.1×10^{-17}	1.5×10^{-17}	0.27	0.3	0.2	1.612	1.46×10^{-10}
AMALGAM-SO	9.3×10^{-13}	9.3×10^{-13}	2.8×10^{-14}	0.39	0.377	2.98	2.83	8.5×10^{-12}

† ϕ, porosity; S_{ini}, initial saturation; α and n, van Genuchten fitting parameters; D^*, porous medium diffusion coefficient.

TABLE 4. Ranges of parameters† used in the AMALGAM-SO calibration simulations.

Statistic	k_h	k_z	ϕ	S_{ini}	α	n	D^*
	m^2				1/m		m^2/s
Minimum	1.0×10^{-18}	1.0×10^{-18}	0.26	0.14	0.1	1.05	1×10^{-12}
Maximum	1.0×10^{-10}	1.0×10^{-10}	0.47	0.35	4.0	3.00	1×10^{-10}

† k_h and k_z, saturated permeabilities; ϕ, porosity; S_{ini}, initial saturation; α and n, van Genuchten fitting parameters; D^*, porous medium diffusion coefficient.

TABLE 5. Ranges of parameters† used in the Shuffled Complex Evolution Metropolis (SCEM-UA) calibration simulations.

Statistic	k_h	k_z	ϕ	θ_{ini}	α	n	D^*
	m^2				1/m		m^2/s
Minimum	1.0×10^{-14}	1.0×10^{-15}	0.26	0.10	0.1	1.05	1×10^{-12}
Maximum	3.2×10^{-13}	3.2×10^{-13}	0.47	0.15	4.0	2.00	1×10^{-10}

† k_h and k_z, saturated permeabilities; ϕ, porosity; S_{ini}, initial saturation; α and n, van Genuchten fitting parameters; D^*, porous medium diffusion coefficient.

The optimum parameter values derived with AMALGAM-SO (Table 3) led to an RMSE of about 0.02, which is better than the solution found with manual calibration but not very different in terms of a modeled breakthrough curve (Fig. 6). If we were to allow uncertainty in the measured data on the order of C/C_o = 0.01, these two very different parameter sets could easily be considered equally acceptable. Because the parameters found in the AMALGAM-SO optimization were quite different from those used in the manual calibration, we realized that the solution space might have many solutions with RMSE values close to the global optimum but with a diverse set of parameter combinations. Such complex solution spaces should be further investigated with an algorithm that facilitates converging to a distribution of parameter combinations rather than the global optimum only (e.g., Vrugt et al., 2003b).

Parameter Space Exploration Using the Shuffled Complex Evolution Metropolis Algorithm

Using a parallel version of the SCEM-UA optimization algorithm (Vrugt et al., 2006), we performed >33,000 FEHM model simulations to more completely explore the parameter space and to better understand the differences between the constant porous medium diffusion coefficient model (CD) and the MQ and CW models for diffusion as a function of water content. The SCEM-UA algorithm converges to the posterior probability distribution function of the parameters within a Bayesian framework, and thus finds multiple different solutions that are within an acceptable distance from the traditional best solution. Table 5 lists the ranges of the parameters used in the SCEM-UA optimization. The ranges were chosen based on the results of the AMALGAM-SO optimization, with further constraints placed by measured values of permeability and the van Genuchten n parameter. To increase efficiency, the permeability bounds were made consistent with their measured ranges presented in Tseng et al. (2003). Thus, the upper bound of permeability was limited to 3.2×10^{-13} m^2, only slightly higher than the highest measured value of 2.7×10^{-13} m^2. Bounds were also placed on initial water content (θ_{ini}) and porosity (ϕ) and the initial saturation value used in the FEHM was calculated from $S_{ini} = \theta_{ini}/\phi$. This ensured that θ_{ini}, could not deviate from the in situ measured water content at the Busted Butte field site.

TABLE 6. Root mean square error values for the simulations using the finite element heat and mass transfer porous flow simulator (FEHM).

Simulation	RMSE	No. of distinct solutions	Total no. of FEHM simulations
Base (Millington–Quirk)	0.090	1	1
Base (Conca–Wright)	0.142	1	1
Manual optimization	0.026	1	10
AMALGAM-SO (constant diffusion)	0.020	1	12,000
SCEM-UA (constant diffusion)	0.021	1284	10,780
SCEM-UA (Millington–Quirk)	0.023	731	7,000
SCEM-UA (Conca–Wright)	0.069	924	15,840

Table 6 lists summary statistics of the SCEM-UA optimization for the CW, MQ, and CD models. The listed RMSE values correspond to the best value found with SCEM-UA. In addition, Fig. 6 shows the best results from the SCEM-UA optimization for the three diffusion models. Note that the CW model is too diffusive and has a simulated breakthrough curve that overpredicts the measured Br breakthrough data at times less than 60 d while underpredicting the measured breakthrough data at later times. Indeed, all 924 different parameter combinations derived with SCEM-UA using the CW model have an RMSE that >0.07. This finding demonstrates that the CW model is not appropriate for the conditions and scale of the tracer test.

In contrast to the CW model, both the CD and MQ models yielded very good matches to the observed Br concentration data, with RMSE values of 0.021 and 0.023, respectively (Table 6). The CD model produced 1284 different solutions using a total of 10,780 SCEM-UA FEHM model evaluations, while the MQ model produced 731 different solutions after sampling 7000 parameter combinations (Table 6).

To better understand the differences between the CD and MQ models, consider Fig. 10, which plots the average quadratic

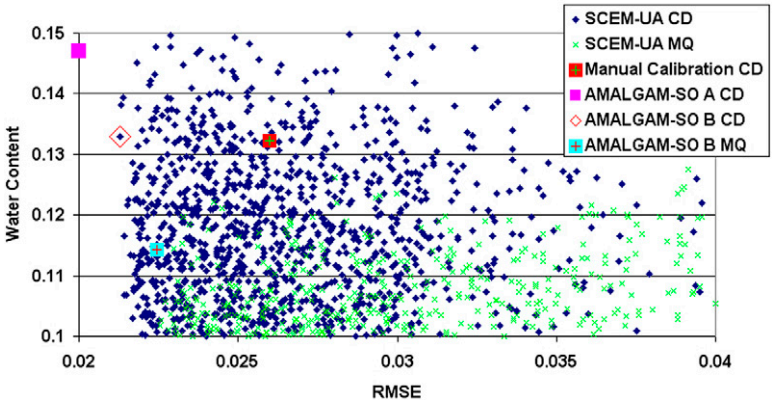

FIG. 10. Volumetric water content plotted against the RMSE for the Shuffled Complex Evolution Metropolis (SCEM-UA) simulations using constant diffusion (CD) and the Millington–Quirk (MQ) diffusion model. The manual calibration values are plotted for comparison. The AMALGAM-SO A CD point is the optimized solution found with the bounds specified in Table 4, while the two AMALGAM-SO B points are the optimized solutions found using the same parameter ranges as for the SCEM-UA cases.

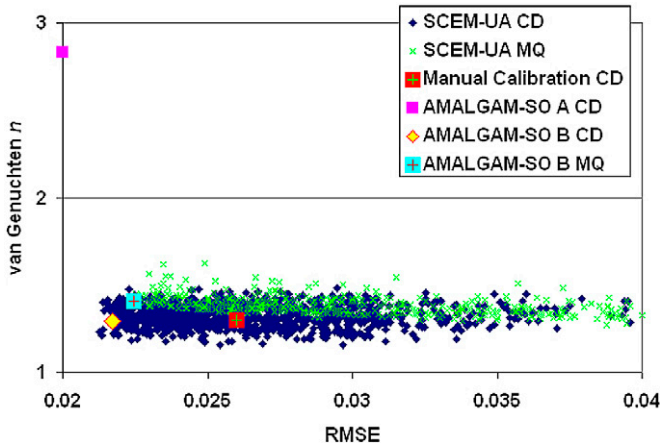

FIG. 11. The van Genuchten *n* parameter plotted against the RMSE for the Shuffled Complex Evolution Metropolis (SCEM-UA) simulations using constant diffusion (CD) and the Millington–Quirk (MQ) diffusion model. The manual calibration values are plotted for comparison. The AMALGAM-SO A CD point is the optimized solution found with the bounds specified in Table 4, while the two AMALGAM-SO B points are the optimized solutions found using the same parameter ranges as for the SCEM-UA cases.

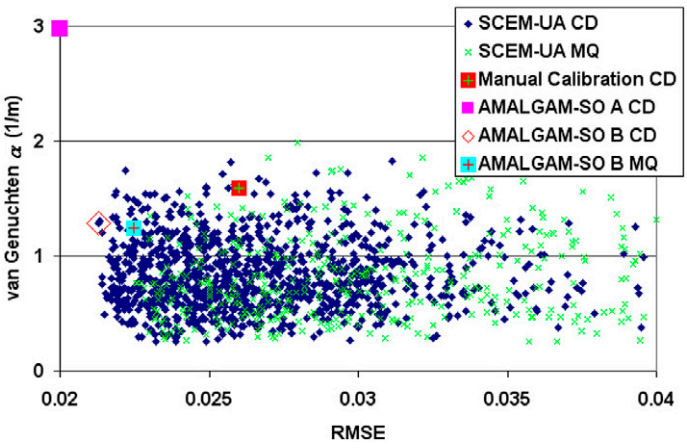

FIG. 12. The van Genuchten α parameter plotted against the RMSE for the Shuffled Complex Evolution Metropolis (SCEM-UA) simulations using constant diffusion (CD) and the Millington–Quirk (MQ) diffusion model. Manually calibrated values and AMALGAM-SO results are plotted for comparison. The AMALGAM-SO A CD point is the optimized solution found with the bounds specified in Table 4, while the two AMALGAM-SO B points are the optimized solutions found using the same parameter ranges as for the SCEM-UA cases.

error (RMSE) in simulated Br concentration against the optimized volumetric water content (θ_{ini}). Note that the CD and MQ models span a very similar range of RMSE values, but that the 391 different MQ solutions derived with the SCEM-UA algorithm have a volumetric water content that is well below the mean measured θ_{ini} of about 0.13. On the contrary, the CD-simulated water content values closely mimic the in situ soil moisture observations. This illustrates that the CD model is more representative of the field conditions at Busted Butte. For comparison, the manual calibration result and AMALGAM-SO realization with large parameter bounds discussed above (labeled AMALGAM-SO A CD) are shown in Fig. 10. Also shown in Fig. 10 are two AMALGAM-SO results (labeled AMALGAM-SO B CD and AMALGAM-SO B MQ) that used the same bounds as were used in the SCEM-UA analysis. These final two points plot exactly on top of the best RMSE found using the SCEM-UA algorithm, and show that the two algorithms converge to the same optimum result when using the same parameter bounds.

To provide insight into the sampled parameter space, Fig. 11 and 12 present dotty plots of the sampled value of *n* and α in the van Genuchten water retention function vs. the RMSE value for the CD and MQ models. Also included in these figures are the optimized values used in the manual and AMALGAM-SO calibrations. The CD and MQ models are in good agreement about the optimized ranges and correlations of the van Genuchten α and *n* parameters, which suggests that the shape of the retention function at the Busted Butte field site is well defined, irrespective of the choice of the underlying diffusion model, providing confidence in our results.

Figure 13 shows a two-dimensional scatter plot of sampled van Genuchten α and *n* values using the SCEM-UA algorithm for the CD and MQ models. The manual calibration and AMALGAM-SO results are also included. In addition, we plotted the optimized solution of a separate SCEM-UA calibration using the measured retention data from rock core samples. The plot depicts an almost linear correlation between α and *n*, but with quite some scatter. Interestingly, the AMALGAM-SO solution

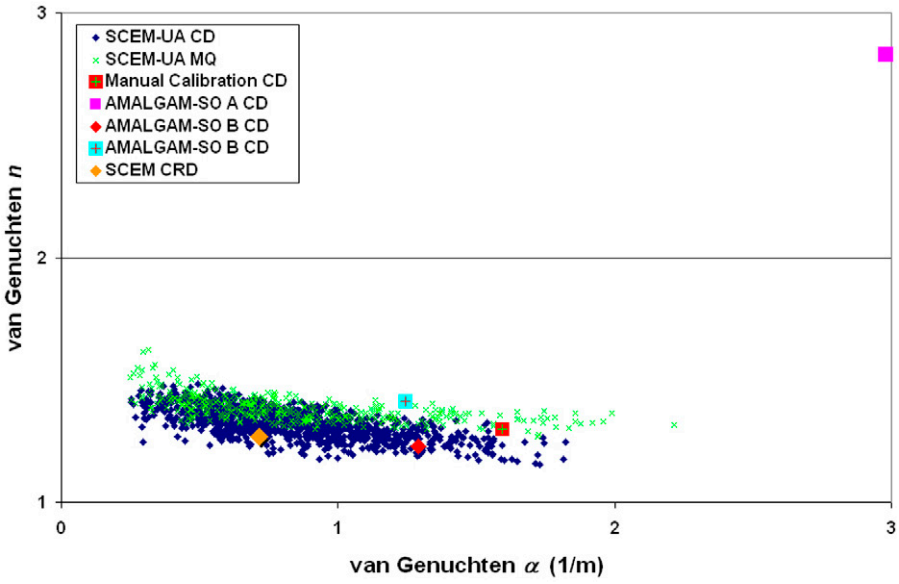

FIG. 13. The van Genuchten *n* vs. α parameters for the Shuffled Complex Evolution Metropolis (SCEM-UA) simulations using constant diffusion (CD) and the Millington–Quirk (MQ) diffusion model. The manual calibration values are plotted for comparison. The AMALGAM-SO A CD point is the optimized solution found with the bounds specified in Table 4, while the two AMALGAM-SO B points are the optimized solutions found using the same parameter ranges as for the SCEM-UA cases. Additionally, the results from a separate SCEM-UA calibration of the retention data (CRD) are shown.

with large parameter bounds (labeled AMALGAM-SO A CD) does not plot anywhere near the high-density region found with the SCEM-UA algorithm and appears physically unrealistic considering the optimized values of α and n separately obtained from rock core samples. These results reinforce the importance of constrained optimization, with parameter bounds dictated by values determined using independent measurements.

Figure 14 plots the optimized horizontal and vertical permeability (k_h and k_v) for the same solutions shown in Fig. 10 to 13. The CD and MQ models show good agreement because values are aligned along the $k_h = k_v$ line. The MQ model predicts that k_v should be slightly less than k_h, while the CD model predicts that k_v should be slightly higher than k_h. Seemingly, the horizontal and vertical permeability are of very similar magnitude, something that is to be expected given the properties of the volcanic tuff at the Busted Butte field site. In contrast, the AMALGAM-SO solution with large parameter bounds (labeled AMALGAM-SO A CD) resulted in a horizontal permeability that is 1.5 orders of magnitude greater than the vertical permeability. This graph also helps to justify our use of tighter bounds on the permeability ranges, since very few values lie off the perfectly linear 1:1 correlation, and as vertical permeability increased above 3×10^{-13} m^2, advective transport was too rapid and not consistent with the experimental data.

Finally, we present D^* as a function of the RMSE for the CD and MQ models. Figure 15 shows that the CD model assigns a very high probability to the diffusion coefficient at the Busted Butte field site being smaller than 2×10^{-11} m^2/s (75%), while the MQ model more evenly spreads the probability mass of D^* between 4×10^{-11} and 1×10^{-10} m^2/s. We conclude that both models give a very good fit to the observed Br concentration data at the Busted Butte field site but result in quite different optimized values and distributions of D^*. This is an important finding that deserves careful interpretation. Interestingly, we found no correlation between D^* and either α or k_v, implying that the trade-off between advective and diffusive transport is likely to be controlled by more complex parameter interactions.

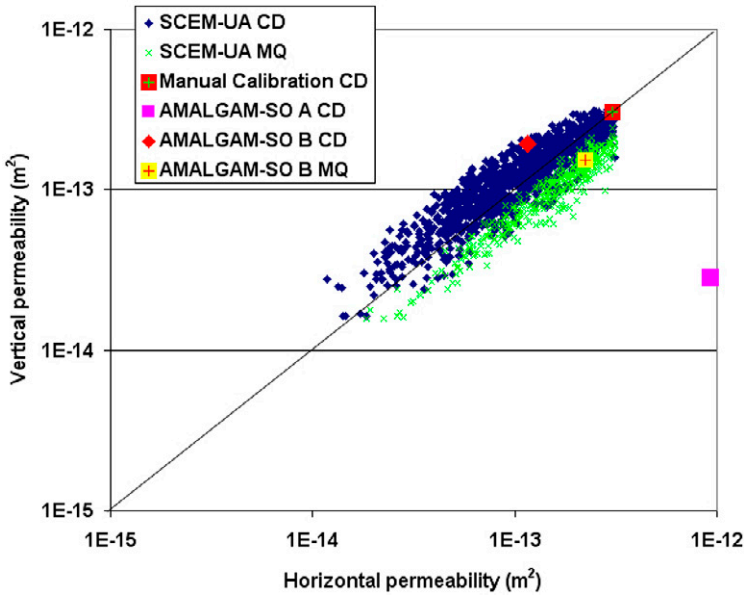

FIG. 14. Vertical vs. horizontal permeability for the Shuffled Complex Evolution Metropolis (SCEM-UA) simulations with RMSE <0.04 using constant diffusion (CD) and the Millington–Quirk (MQ) diffusion model. The manual calibration values are plotted for comparison. The AMALGAM-SO A CD point is the optimized solution found with the bounds specified in Table 4, while the two AMALGAM-SO B points are the optimized solutions found using the same parameter ranges as for the SCEM-UA cases. The diagonal line highlights the region where horizontal and vertical permeability are equal.

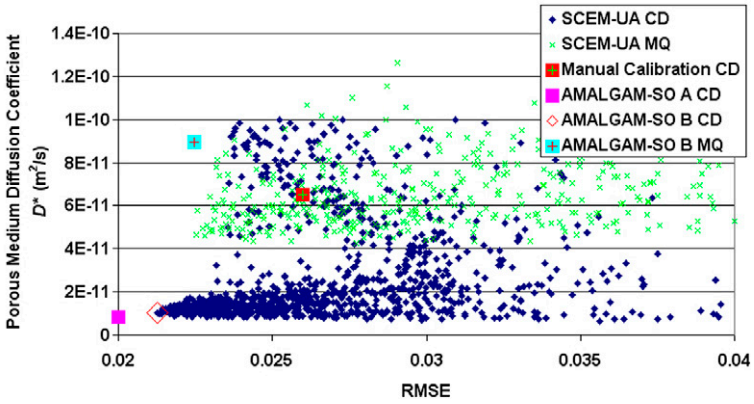

FIG. 15. The porous medium diffusion coefficient vs. RMSE for the Shuffled Complex Evolution Metropolis (SCEM-UA) simulations using constant diffusion (CD) and the Millington-Quirk (MQ) diffusion model. The manual calibration values are plotted for comparison. The AMALGAM-SO A CD point is the optimized solution found with the bounds specified in Table 4, while the two AMALGAM-SO B points are the optimized solutions found using the same parameter ranges as for the SCEM-UA cases.

Discussion

Although the AMALGAM-SO and manual calibration parameter estimates gave good matches to the measured Br concentration data, these two approaches do not provide insight into parameter uncertainty. The SCEM-UA algorithm provides a methodology to assess ranges of individual parameters that can be considered acceptable given the experimental data for calibration. Ranges derived from a SCEM-UA analysis such as this could be useful in large-scale Monte Carlo style performance assessments (PA) (Robinson et al., 2003). For example, Fig. 11 suggests that a very narrow range of the van Genuchten parameter n would be appropriate, while Fig. 12 reduces the original range in α by more than a factor of two. Figure 13 provides justification for correlating α and n, thus reducing the sampling needs in Monte Carlo simulations. Figure 14 shows that the AMALGAM-SO A CD optimization, with higher bounds permitted on n, led to an optimized solution with significant permeability anisotropy; however, when the bounds on n were tightened to reflect the site data, no significant anisotropy in permeability was found to fit the breakthrough data using any of the optimization techniques. Thus, Fig. 14 gives strong evidence that allowing large anisotropy in permeability is not justified and also suggests a correlation that could reduce parameter sampling needs for PA calculations. Figure 15 shows that two conceptual models for the porous medium diffusion coefficient would need to be used in PA calculations if one wanted to appropriately capture the underlying uncertainty in transport dominated by diffusion. This is consistent with approaches such

as Bayesian model averaging that are currently emerging in the hydrologic literature (Neuman, 2003; Meyer et al., 2007; Vrugt and Robinson, 2007b).

Although the CW and MQ models provide accurate descriptions of flow and transport at very small spatial scales and steady-state conditions, the transient nature and 25-cm transport distance of the Phase 1B experiment has revealed a possible shortcoming in these model formulations. We posit that the porous medium diffusion coefficient may be inversely related to the experimental length scale. This would explain why the CW measurements done on very small samples yielded consistently larger diffusion coefficients than MQ estimates done on larger samples. Following logic similar to that used to justify the increase in dispersivity that occurs as the flow path length increases (Gelhar et al., 1992), we conjecture that diffusion may be reduced at larger scales because harmonic averaging of heterogeneity in longer paths puts more weight on areas of low diffusivity, thus increasing the length of the tortuous path needed for a molecule to diffuse through the subsurface. This idea is supported by Kwicklis et al. (2006), who also found that MQ and CW were overly diffusive and their modeling required a lower D^* to fit long-term records of stable isotopes and Cl^- from the subsurface of the Nevada Test Site. Support for the use a harmonically averaged diffusion coefficient in the direction of transport can be found by analogy to the well-known harmonic permeability relationship in porous flow, because both diffusive transport and porous flow solve the same diffusion equation.

Simulations that pinpoint the effects of diffusion and advection show that both the advective and diffusive mechanisms are very important for solute transport in the Phase 1B experiment (Fig. 7–9). Modeling results from the Phase 2 tracer test showed that the system was insensitive to changes in the diffusion coefficient at scales >1 m (Tseng et al., 2003). The insensitivity of Phase 2 to changes in the Br diffusion coefficient is related to the higher flow velocities and one-dimensional flow field, as discussed above. Phase 1A (Robinson and Bussod, 2000) was a more qualitative experiment and did not have the spatial and temporal resolution to determine an accurate effective diffusion coefficient. Therefore, the Phase 1B experiment provides important insight that could not have been obtained from either Phase 1A or Phase 2 and highlights the need to collect experimental data at different spatial scales.

Finally, this study shows that unsaturated transport problems may have many near-optimum parameter combinations. To ensure that uncertainty is adequately captured, one should therefore use a range of parameter values in model predictions of long-term flow and transport.

Conclusions

Optimized hydraulic parameters from laboratory-derived retention functions of rock core samples provided a good description of Br breakthrough data at the collector located directly beneath the injector. The simulations showed that both capillary forces and gravity control the advective flux, while molecular diffusion at this site is dependent on the highly tortuous pathways that form in unsaturated rocks. The scale of the experiment was such that we were clearly able to differentiate between diffusion and advection.

Our optimization results with AMALGAM-SO and SCEM-UA provide the necessary information to be able to draw sound conclusions about which diffusion models were best supported given the experimental data at the Busted Butte field site. Moreover, the posterior distribution derived with the SCEM-UA algorithm provides important insight into parameter uncertainty, and correlation, and can be used to efficiently generate model output predictive distributions. Optimization results lying far from independently measured hydrologic data show the importance of constraining search algorithms to sample values of parameters that are representative of field measurements.

All our simulations support the conclusion that tracer breakthrough in this experiment cannot be described adequately using the CW model to calculate the unsaturated diffusion coefficient as a function of porosity and volumetric water content. The MQ model provided an excellent match to the observed Br concentration data; however, a lower constant porous medium diffusion model, with a coefficient of approximately 1×10^{-11} m^2/s, also yielded a significant cluster of local solutions. This suggests that at the scale of the experiment, diffusion may be reduced below values calculated using MQ. Reducing porous medium diffusion coefficients in partially saturated rock and soil could have broad implications for understanding contaminant transport in diffusion-controlled environments in the subsurface.

Acknowledgments

This paper is dedicated in honor and loving memory of Wendy Soll, whose vision and guidance form the foundation of this paper—fare thee well, Wendy. The experimental design, data collection, and initial modeling were supported by the Yucca Mountain Site Characterization Program Office as part of the Civilian Radioactive Waste Management Program. This project is managed by the U.S. Department of Energy, Yucca Mountain Site Characterization Project. Special thanks to Gilles Bussod, without whom the tracer test would not have been possible. We thank T. Stockton of Neptune Inc. for providing the curve fit to the Conca–Wright diffusion as a function of volumetric water content data, and gratefully acknowledge Michael Sully and John Tauxe for insightful discussions into the dependence of diffusion on volumetric water content. We also thank Bruce Robinson for many conversations that helped to improve this work. We highly appreciate the computer support provided by the SARA center for parallel computing at the University of Amsterdam, the Netherlands. J.A. Vrugt was supported by a J. Robert Oppenheimer Fellowship of the Los Alamos Postdoctoral Program. YMP project review led by Ming Zhu helped refine our arguments significantly.

References

Anghel, I., H.J. Turin, and P.W. Reimus. 2002. Lithium sorption to Yucca Mountain tuffs. Appl. Geochem. 17:819–824.

Bear, J., and A. Verruijt. 1989. Modeling groundwater flow and pollution. D. Reidel Publ. Co., Dordrecht, the Netherlands.

Bechtel SAIC Company. 2004a. Radionuclide transport models under ambient conditions. DOC.20041101.0002, MDL-NBS-HS-000008 Rev 2. BSC, Las Vegas, NV.

Bechtel SAIC Company. 2004b. In situ field testing of processes. ANL-NBS-HS-000005 REV 03. 1180. BSC, Las Vegas, NV.

Bussod, G.Y, K. Coen, and R.C. Eckhardt. 1998. LA testing status report: Busted Butte unsaturated zone transport test. YMP Deliverable SPU85M4. Los Alamos Natl. Lab., Los Alamos, NM.

Clennell, B. 1997. Tortuosity: A guide through the maze. p. 299–344. *In* M.A. Lovell and P.K. Harvey (ed.) Developments in petrophysics. Geol. Soc. Spec. Publ. 122. Geol. Soc. London.

Conca, J.L., and J. Wright. 2000. Aqueous diffusion in the vadose zone. p. 796–797. *In* B.B. Looney and R.W. Falta (ed.) The vadose zone. Battelle Press, Columbus, OH.

Fetter, C.W. 1999. Contaminant hydrogeology. 2nd ed. Prentice Hall, Upper Saddle River, NJ.

Flint, L.E. 1999. Laboratory and centrifuge measurements of physical and hydraulic properties of core samples from Busted Butte boreholes. Yucca Mountain Project-U.S. Geological Survey Technical Data Record, DTN: GS990708312242.008. Yucca Mountain Project.

Gelhar, L.W., C. Welty, and K.R. Rehfeldt. 1992. A critical review of data on field-scale dispersion in aquifers. Water Resour. Res. 28:1955–1974.

Ho, C., and S. Webb. 1998. Review of porous media enhanced vapor-phase diffusion mechanisms, models, and data: Does enhanced vapor-phase diffusion exist? J. Porous Media 1:71–92.

Jury, W.A., and W.R. Gardner. 1991. Soil physics. 5th ed. John Wiley & Sons, New York.

Karimi, A.A., W.J. Farmer, and M.M. Cliath. 1987. Vapor-phase diffusion of benzene in soil. J. Environ. Qual. 16:38–43.

Kwicklis, E.M., A.V. Wolfsberg, P.H. Stauffer, M.A. Walvrood, and M.J. Sully. 2006. Multiphase multicomponent parameter estimation for liquid and vapor fluxes in deep arid systems using hydrologic data and natural environmental tracers. Vadose Zone J. 5:924–950.

Liu, H.H., G.S. Bodvarsson, and G. Zhang. 2005. Scale dependency of the effective matrix diffusion coefficient. Vadose Zone J. 3:312–315.

Meyer, P.D., M. Ye, M.L. Rockhold, S.P. Neuman, and K.J. Cantrell. 2007. Combined estimation of hydrogeologic conceptual model, parameter, and scenario uncertainty with application to uranium transport at the Hanford Site 300 Area. NUREG/CR-6940, PNNL-16396. U.S. Nucl. Regul. Commiss., Washington, DC.

Millington, R.J., and J.P. Quirk. 1961. Permeability of porous solids. Trans. Faraday Soc. 57:1200–1207.

Neeper, D.A., and P.H. Stauffer. 2005. Unidirectional gas flow in soil porosity resulting from barometric pressure cycles. J. Contam. Hydrol. 78:281–289.

Neuman, S.P. 2003. Maximum likelihood Bayesian averaging of alternative conceptual-mathematical models. Stochastic Environ. Res. Risk Assess. 17:291–305.

Robinson, B.A., and G.Y. Bussod. 2000. Radionuclide transport in the unsaturated zone at Yucca Mountain: Numerical model and preliminary field observations. p. 323–336. *In* B. Faybishenko et al. (ed.) Dynamics of fluids in fractured rocks: Concepts and recent advances. Geophys. Monogr. 122. Am. Geophys. Union, Washington, DC.

Robinson, B.A., C. Li, and C.K. Ho. 2003. Performance assessment model development and analysis of radionuclide transport in the unsaturated zone, Yucca Mountain, Nevada. J. Contam. Hydrol. 62–63:249–268.

Schaefer, C.E., R.R. Arands, H.A. van der Sloot, and D.S. Kosson. 1995. Prediction and experimental validation of liquid-phase diffusion resistance in unsaturated soils. J. Contam. Hydrol. 20:145–166.

Schaefer, C.E., R.R. Arands, H.A. van der Sloot, and D.S. Kosson. 1997. Modeling of the gaseous diffusion coefficient through unsaturated systems. J. Contam. Hydrol. 29:1–21.

Science and Engineering Associates. 1992. The use of absorbent materials to collect in situ vadose zone liquids. Topical Rep. SEATR-92–01. SEA, Santa Fe, NM.

Scott, R.B., and J. Bonk. 1984. Preliminary geologic map of Yucca Mountain, Nye County, Nevada with geologic sections (1:12000). USGS-OFR-84-494. USGS, Reston, VA.

Stauffer, P.H. 2006. Flux flummoxed. Ground Water 44:125–128.

Stauffer, P.H., K.H. Birdsell, M.S. Witkowski, and J.K. Hopkins. 2005. Vadose zone transport of 1,1,1-trichloroethane: Conceptual model validation through numerical simulation. Vadose Zone J. 4:760–773.

Stauffer, P.H., and N.D. Rosenberg. 2000. Vapor phase transport at a hillside landfill. Environ. Eng. Geosci. 6:71–84.

Stauffer, P.H., and W.J. Stone. 2005. Surface water–groundwater connection at the Los Alamos Canyon Weir Site: 2. Modeling of tracer test results. Vadose Zone J. 4:718–728.

Stuckless, J.S., and W.W. Dudley. 2002. The geohydrologic setting of Yucca Mountain, Nevada. Appl. Geochem. 17:659–682.

Trease, H., D. George, C.W. Gable, J. Fowler, A. Kuprat, and A. Khamyaseh. 1996. The X3D grid generation system. *In* B.K. Soni et al. (ed.) Numerical grid generation in computational fluid dynamics and related fields. Eng. Res. Ctr., Mississippi State Univ. Press, Mississippi State, MS.

Tseng, P.-H., and G.Y. Bussod. 2001. Evaluation of the filter paper technique for in-situ sampling of solute transport in unsaturated soils and tuffs. Water Resour. Res. 37:1913–1928.

Tseng, P.-H., W.E. Soll, C.W. Gable, H.J. Turin, and G.Y. Bussod. 2003. Modeling unsaturated flow and transport processes at the Busted Butte Field Test Site, Nevada. J. Contam. Hydrol. 62–63:303–318.

Turin, H.J., A.R. Groffman, L.E. Wolfsberg, J.L. Roach, and B.A. Strietelmeier. 2002. Tracer and radionuclide sorption to vitric tuffs of Busted Butte, Nevada. Appl. Geochem. 17:825–836.

Turin, H.J., C.L. Jones, A.R. Groffman, S. Dalvit, S.D. Dunn, W.E. Lowry, and W.E. Soll. 2004. Collection of unsaturated-zone water samples for tracer analysis: Evaluation of an inverting membrane technique. Ground Water Monit. Rev. 24:95–101.

van Genuchten, M.Th. 1980. A closed form equation for predicting hydraulic conductivity of unsaturated soils. Soil Sci. Soc. Am. J. 44:892–898.

Viswanathan, H.S., B.A. Robinson, A.J. Valocchi, and I.R. Triay. 1998. A reactive transport model of neptunium migration from the potential repository at Yucca Mountain. J. Hydrol. 209:251–280.

Vrugt, J.A., W. Bouten, H.V. Gupta, and J.W. Hopmans. 2003b. Toward improved identifiability of soil hydraulic parameters: Suitable parametric model. Vadose Zone J. 2:98–113.

Vrugt, J.A., H.V. Gupta, W. Bouten, and S. Sorooshian. 2003a. A Shuffled Complex Evolution Metropolis algorithm for optimization and uncertainty assessment of hydrologic model parameters. Water Resour. Res. 39(8):1201, doi:10.1029/2002WR001642.

Vrugt, J.A., B.O. Nuallain, B.A. Robinson, W. Bouten, S.C. Dekker, and P.M.A. Sloot. 2006. Application of parallel computing to stochastic parameter estimation in environmental models. Comput. Geosci. 32:1139–1155.

Vrugt, J.A., and B.A. Robinson. 2007a. Improved evolutionary optimization from genetically adaptive multimethod search. Proc. Natl. Acad. Sci. 104:708–711.

Vrugt, J.A., and B.A. Robinson. 2007b. Treatment of uncertainty using ensemble methods: Comparison of sequential data assimilation and Bayesian model averaging. Water Resour. Res. 43:W01411, doi:10.1029/2005WR004838.

Vrugt, J.A., B.A. Robinson, and J.M. Hyman. 2009. Self-adaptive multimethod search for global optimization in real-parameter spaces. IEEE Trans. Evol. Comput. (in press).

Vrugt, J.A., P.H. Stauffer, Th. Wöhling, B.A. Robinson, and V.V. Vesselinov. 2008. Inverse modeling of subsurface flow and transport properties using recent advances in global optimization, parallel computing, and sequential data assimilation. Vadose Zone J. 7:843–864.

Zyvoloski, G.A. 2007. FEHM: A control volume finite element code for simulating subsurface multi-phase multi-fluid heat and mass transfer. Rep. LAUR-07–3359. Los Alamos Natl. Lab., Los Alamos, NM.

Zyvoloski, G.A., B.A. Robinson, Z.V. Dash, and L.L. Trease. 1997. Summary of the models and methods for the FEHM application: A finite-element heat- and mass-transfer code. Rep. LA-13307-MS. Los Alamos Natl. Lab., Los Alamos, NM.